Topography of the salar de Uyuni, Bolivia from kinematic GPS

Adrian A. Borsa,[1] Helen A. Fricker,[1] Bruce G. Bills,[1,2] Jean-Bernard Minster,[1] Claudia C. Carabajal[2,3] and Katherine J. Quinn[4]

[1] *Institute of Geophysics and Planetary Physics, Scripps Institution of Oceanography, University of California at San Diego, La Jolla, California, USA.*
E-mail: aborsa@ucsd.edu
[2] *Planetary Geodynamics Laboratory, NASA Goddard Space Flight Center, Greenbelt, Maryland, USA*
[3] *Sigma Space Corporation, Lanham, Maryland, USA*
[4] *Jet Propulsion Laboratory, California Institute of Technology, Pasadena, California, USA*

SUMMARY
The salar de Uyuni in the Bolivian Andes is the largest salt flat on Earth, exhibiting less than 1 m of vertical relief over an area of 9000 km^2. We report on a kinematic Global Positioning System (GPS) survey of a 45-by-54 km area in the eastern salar, conducted in September 2002 to provide ground truth for the Ice Cloud and land Elevation Satellite (ICESat) mission. GPS post-processing included corrections for long-period GPS noise that significantly improved survey accuracy. We fit corrected GPS trajectories with 2-D Fourier basis functions, from which we created a digital elevation model (DEM) of the surface whose absolute accuracy we estimate to be at least 2.2 cm RMSE. With over two magnitudes better vertical resolution than the Shuttle Radar Topography Mission data, this DEM reveals decimetre-level topography that is completely absent in other topographic data sets. Longer wavelengths in the DEM correlate well with mapped gravity, suggesting a connection between broad-scale salar topography and the geoid similar to that seen over the oceans.

Key words: Space geodetic surveys; Gravity anomalies and Earth structure; Geomorphology; South America.

1 INTRODUCTION

Bolivia's salar de Uyuni is the largest salt flat on Earth, a 9000 km^2 expanse of halite at 4 km above sea level in the Andean Altiplano. The salar is the lowest point of an internal drainage basin that has undergone many cycles of inundation and evaporation throughout the late Quaternary (Argollo & Mourguiart 2000; Fornari *et al.* 2000). Interlayered salt and mud deposits reaching depths of hundreds of metres in the centre of the salar (Baker *et al.* 2001; Fritz *et al.* 2004) are relics of a long history of sedimentation during lacustrine phases followed by the deposition of halite in the lower reaches of the basin when the lakes retreated and evaporated (Risacher & Fritz 2000). Although the current dry period has persisted for at least 8000 yr (Sylvestre *et al.* 1999), hydrological activity continues in the form of periodic flooding which regenerates the surface via the dissolution and redeposition of salt (Lowenstein & Hardie 1985) and appears to be responsible for maintaining the salar's extraordinary smoothness.

As an extremely broad and flat terrestrial surface, the salar de Uyuni is an ideal reference target for Earth-orbiting altimeters. Each overflight of the salar can yield hundreds of altimeter ground returns whose waveforms are unmodified by topography and whose reported elevations vary minimally across the surface. Validation of altimeter measurements requires far better vertical resolution than is provided by existing topographic data sets, however. Radar al-

timeters such as Envisat and TOPEX/Poseidon (e.g. Fu *et al.* 1994) and the laser altimeter aboard NASA's Ice Cloud and land Elevation Satellite (ICESat) (Schutz *et al.* 2005) can measure the elevation of flat surfaces to within 5 cm rms, which is two orders of magnitude better than the 6.2 m (90 per cent confidence level) accuracy of Shuttle Radar Topography Mission (SRTM) over South America (Rodriguez *et al.* 2005).

The motivation for this paper was a kinematic Global Positioning System (GPS) survey of the salar de Uyuni carried out in September 2002 to provide ground truth for the ICESat laser altimeter (see Fricker *et al.* 2005). Preliminary analysis of the GPS data showed that the total vertical relief over our 2000 km^2 survey area was less than 80 cm, half of which could be accounted for by the planar trend of the surface. Evidence of broad-scale topographic structure at the centimetre to decimetre level inspired us to apply a new technique for correcting the GPS time-series in order to resolve surface features partly obscured by long-period noise. This signal-to-noise problem also led us to adopt a non-traditional method of DEM generation that allowed us to better quantify the spatial error statistics of our data. Our DEM of the salar de Uyuni ultimately reveals extensive, subtle topography that is invisible to observers on the surface, yet which has implications for practical applications such as satellite altimeter calibration/validation as well as for basic research in salt flat hydrology and geomorphology.
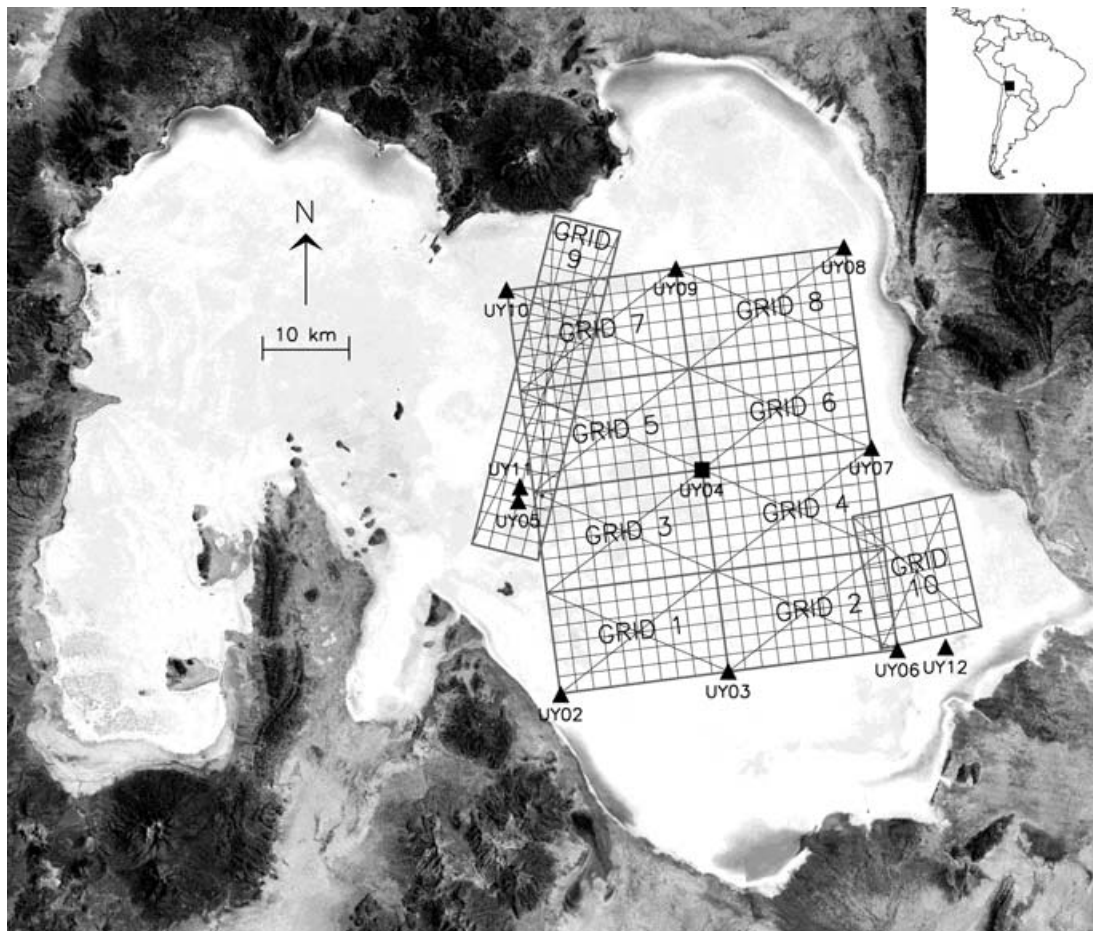
Figure 1. Landsat image of the salar de Uyuni, showing the major components of the GPS survey. Fixed GPS sites UY02–UY12 are shown as triangles, the GPS reference site UY04 is shown as a square, and Grids 1–10 are indicated by their survey tracks. This image shows the salar during the dry season, with surface water confined to the darker areas at the perimeter of the salt. During the wet season, the entire surface is often flooded.

2 SURVEY DESCRIPTION

2.1 Kinematic survey design

We conducted our survey of the salar de Uyuni over 6 d in September 2002 in two vehicles equipped with dual-frequency Ashtech Z-12 GPS receivers and roof-mounted choke ring antennas. The main survey covered a 45-by-54 km area within the eastern lobe of the salar and consisted of eight independently surveyed grids, with two additional grids acquired afterwards along ground tracks of the Envisat and ERS-2 satellites (Fig. 1). Spacing between adjacent tracks within the grids was 2.25 km, and along-track spacing between GPS epochs was approximately 100 m at our 3-s sampling rate. Vehicle antenna heights were measured before and after we drove each grid and were linearly interpolated to each measurement epoch, even though the before/after difference was typically on the order of several millimetres.

2.2 Fixed GPS network

To provide short-baseline contemporaneous data for post-processing the kinematic trajectories, we deployed three GPS fixed stations at sites along the perimeter of the survey area (Fig. 1), moving these stations to new locations as the survey progressed. We attempted to operate fixed stations for at least 24 hr in order to average the daily cycle of signal multipath, although this was not always possible because of time constraints. We also set up a GPS reference station at the centre of the survey area (site UY04), which we operated continuously throughout the survey period.

While the salar is free of above-ground GPS signal scatterers, the uppermost salt layer is typically wet and conductive and is, therefore, a strong GPS reflector. We mounted all fixed antennas a few centimetres above the salt surface in order to minimize the magnitude and frequency of ground-reflection multipath error (Elósegui *et al.* 1995). Electromagnetic coupling with the surface had a negligible effect on the antenna phase centre, as evidenced by the identical surface height estimates we obtained from nearby tripod and ground-mounted antennas.

2.3 GPS post-processing

We obtained daily positions of the reference station at UY04 using the Scripps Orbit and Permanent Array Centre's online SCOUT tool. The permanent stations we used were AREQ, UNSA and TUCU, at an average baseline distance of 635 km. Combining the six daily solutions using inverse-variance weighting, we obtained UY04's coordinates in the International Reference Frame 2000 (ITRF2000) (Table 1).

We post-processed our fixed sites with respect to reference site UY04 using Geodetic Inc.'s 'RTD' package, with double-differenced LC (ionosphere-free) data, a 10° satellite elevation

Table 1. ITRF 2000 ground coordinates for all fixed GPS sites on the salar de Uyuni.

Site ID	WGS84 latitude (°)	WGS84 longitude (°)	WGS84 Elev (m)	Elev σ (cm)
UY02	−20.481128597	−67.598805253	3696.9881	0.81
UY03	−20.451873602	−67.386780503	3696.9230	1.01
UY04	−20.211888829	−67.422529683	3697.2995	1.05
UY05	−20.249937827	−67.654757570	3697.1135	1.29
UY06	−20.424153462	−67.172481456	3697.1087	1.13
UY07	−20.184012344	−67.208250868	3697.2956	1.15
UY08	−19.944182433	−67.245876061	3697.6435	7.82
UY09	−19.971964553	−67.457854540	3697.4134	0.97
UY10	−19.999286761	−67.671819075	3697.3768	1.26
UY11	−20.233916082	−67.652522921	3697.1257	1.02
UY12	−20.419939511	−67.111576193	3697.0858	1.47

The reason that the UY08 standard deviation is so high is that its GPS station's antenna had a defective element.

cut-off, antenna phase-centre mapping, precise IGS ephemerides and zenith delay estimation (Bock *et al.* 2000). RTD solves for antenna position independently at each epoch, which allowed us to identify periods when base stations were experiencing above-average noise levels and were unsuitable for use in post-processing the kinematic trajectory. We estimated site positions from the post-processed time-series using the method described by Bock *et al.* (2000). After removing data from periods with inconsistent ambiguity values, we calculated an initial elevation median and interquartile range (IQR) from the remaining epochs, removed outliers whose elevations were beyond 1.7 IQRs of the median and estimated the site position from the mean of the remaining epochs (Table 1). The 1.7 IQR outlier threshold was chosen because it was the largest value for which elevations at all sites (excepting UY08, which had a faulty antenna) passed the Kolmogorov-Smirnov test for a Gaussian distribution (Press *et al.* 1992). Outlier removal reduced the average elevation standard deviation from 3.2 to 1.8 cm, while negligibly changing the elevation means.

To post-process the kinematic survey data, we used Track (Chen 1998), the Kalman-filter-based kinematic module of the GAMIT package (King & Bock 2006). We employed the same parameters listed above for the fixed sites, used loose (i.e. 100 m epoch^{-1}) constraints on kinematic site motion, fixed all carrier-phase ambiguities to integer values, and excluded from the data any satellite for which an integer ambiguity could not be reliably determined. No attempt was made to correct for anisotropic tropospheric delay due to clouds or water vapour gradients, but we expect that this had minimal impact on the solution because of the clear and stable weather during the survey period. Since Track is capable of incorporating multiple base stations, we used all fixed stations with good noise characteristics (as evaluated from RTD processing) when estimating the trajectories for our survey grids. The result of our three-stage processing chain was the generation of 10 independent kinematic GPS trajectories in the ITRF2000, one for each survey grid.

3 DATA ANALYSIS

3.1 Kinematic GPS accuracy

We estimated the internal consistency of our kinematic solutions using crossover analysis, comparing elevations at the 101 locations on each survey grid (77 on the rectangular tracks and 24 on the diagonals) where the trajectory intersected itself (Ridgway *et al.* 1997;

Borsa *et al.* 2007). Although elevations at crossover locations should be identical in the absence of GPS noise, crossover differences in the eight grids of our main survey ranged from −15 to +15 cm, with an average standard deviation of 4.9 cm. We also compared elevations at 1 km intervals along the overlapping boundaries between adjacent survey grids, generating 173 intergrid differences with a standard deviation of 4.1 cm and values ranging from −14 to +8 cm.

We estimated absolute survey accuracy by comparing vehicle trajectories with known elevations at ground truth 'tiepoints', established wherever the survey vehicle passed within 500 m of a fixed site location. The 47 tiepoint differences in the entire survey had a mean of 2.2 cm, a standard deviation of 4.2 cm, and ranged from −6 to +13 cm. This result is consistent with the crossover and intergrid analyses, all of which show that GPS trajectory error equals or surpasses the subdecimetre vertical resolution required for altimeter validation.

3.2 Correcting kinematic trajectories

A plan view of post-processed survey elevations highlights the problem with GPS noise (Fig. 2a). There are elevation mismatches at many crossover locations, survey lines that are consistently high or low, and elevation biases with respect to nearby ground control sites, all at the cm to dm level. Since we observed similar noise in GPS data from a stationary survey vehicle (Borsa *et al.* 2007) and because time-correlated noise of this magnitude is evident even at permanent stations in established GPS networks (e.g. Bock *et al.* 2000), these anomalies cannot be simply attributed to unmodelled vehicle motion. Instead, they reflect the errors (mainly due to tropospheric delay and signal multipath) remaining in kinematic GPS trajectories after standard GPS post-processing.

To correct the kinematic trajectories, we took advantage of the calculated crossover/tiepoint differences on each grid and the relatively high degree of autocorrelation present in the stationary vehicle time-series. We calculated a GPS noise model for each survey grid using a least-squares inversion that incorporated crossover/tiepoint differences as constraints and enforced model smoothness (i.e. autocorrelation) via first-difference minimization (Borsa *et al.* 2007). The correction we obtained ranges over 25 cm—almost a third of the total vertical relief across the survey—with little difference between points along individual tracks and much larger differences between the more widely time-separated points on adjacent and crossing tracks (Fig. 2b). Subtracting this correction from the kinematic trajectories reduces average crossover RMSE from 4.9 to 0.6 cm and reveals considerable topographic detail that was previously obscured by noise (Fig. 2c).

We validated the corrected GPS trajectories via the 173 intergrid comparisons, which were not part of the inversion and were thus an independent measure of error. Average intergrid RMSE was 4.1 cm before correction and 2.2 cm afterwards. Intergrid differences somewhat overstate the overall survey error since they are made at the edges of survey grids where the noise models are limited by poor crossover difference estimation. We therefore, take 2.2 cm rms to be an upper bound on survey error.

3.3 Creating the digital elevation model (DEM)

Our survey data consist of densely sampled profiles bounding empty regions. Because the data distribution is so non-uniform, this geometry is not ideal for DEM-generating schemes that locally filter and
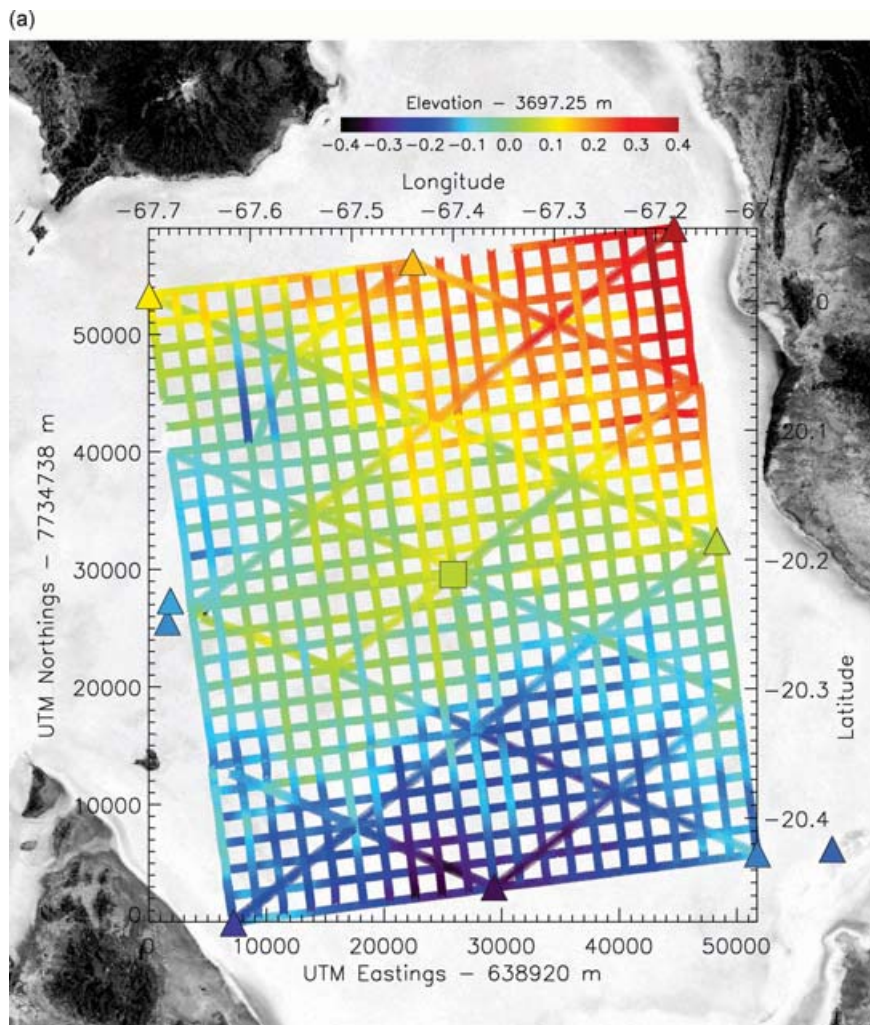
(a)

Figure 2. (a) Standard post-processed GPS trajectories from the salar de Uyuni survey, colour coded for elevation. Fixed sites are shown as coloured triangles. GPS noise is revealed in large crossover differences, survey lines that are anomalously high or low and mismatches with ground elevations at the fixed sites. Correlation of topography within and between survey grids is poor. (b) Plot of the noise model used to correct the raw GPS elevations in (a), colour coded on the same scale. The correction ranges over 25 cm, which is equivalent to almost a third of the vertical relief in the entire survey. Due to model autocorrelation, model differences along individual tracks are small, with larger differences between adjacent and crossing tracks. (c) Kinematic GPS elevations, corrected for GPS noise using the noise model in (b). Compared to (a), crossover differences are minimized and there are no survey tracks showing large excursions in elevation with respect to nearby tracks. Features are well correlated across the survey area, both within and between survey grids.

resample the data to a uniform grid. Filtering and resampling also requires the *a priori* characterization of the spatial statistics of surface, which can be problematic if the topography is not stationary or is anisotropic. Instead, we model the salar surface by fitting the Grid 1–8 elevation data with the 2-D Fourier basis functions (James 1966)

$$h(x, y) = \sum_{k=0}^{m} \sum_{l=0}^{n} a_{k,l} \left[\sin\left(\frac{2\pi x}{L_x}k\right) + i \cos\left(\frac{2\pi x}{L_y}l\right) \right]$$
$$\times \left[\sin\left(\frac{2\pi y}{L_x}k\right) + i \cos\left(\frac{2\pi y}{L_y}l\right) \right], \quad (1)$$

where x and y are the UTM coordinates of the data, L is the size of the fitting region in the coordinate directions and the complex-valued coefficients $a_{k,l}$ are found via least-squares inversion. Implicit in the Fourier expansion in (1) is the periodic extension of the $L_x \times L_y$ data window in the plane. We set $L_x = L_y = 100$ km to create a perimeter around the survey area where all wavelengths in the model

can adjust to discontinuities across the data boundaries and take $m = n$ to ensure that the fit resolution is identical in both directions.

The entire elevation data set has an RMSE about the mean of 14.6 cm. Fitting the data with the Fourier basis set formed by setting $n = 1$ gives a residual misfit of 4.6 cm RMSE. This basis set has a nominal horizontal resolution (L/n) of 100 km. Fitting with the 50 km resolution $n = 2$ basis set reduces the misfit to 2.2 cm RMSE. Additional increments in n improve the fit monotonically (Fig. 3), although unrealistic 'dimpling' of the model within the 2.25-km grid squares occurs when the minimum wavelength in the basis set approaches 6 km (i.e. when $n > 16$).

We use the $n = 15$ model for fitting the survey data because it provides an excellent fit to the data and is well behaved, with no dimpling artefacts in the unsampled regions between survey tracks. Model resolution is 6.7 km in both coordinate directions and the misfit to the data is 0.8 cm RMSE. A plot of model residuals shows no evidence of correlated outliers, which would indicate either topography at wavelengths shorter than 6.7 km or remaining long-period
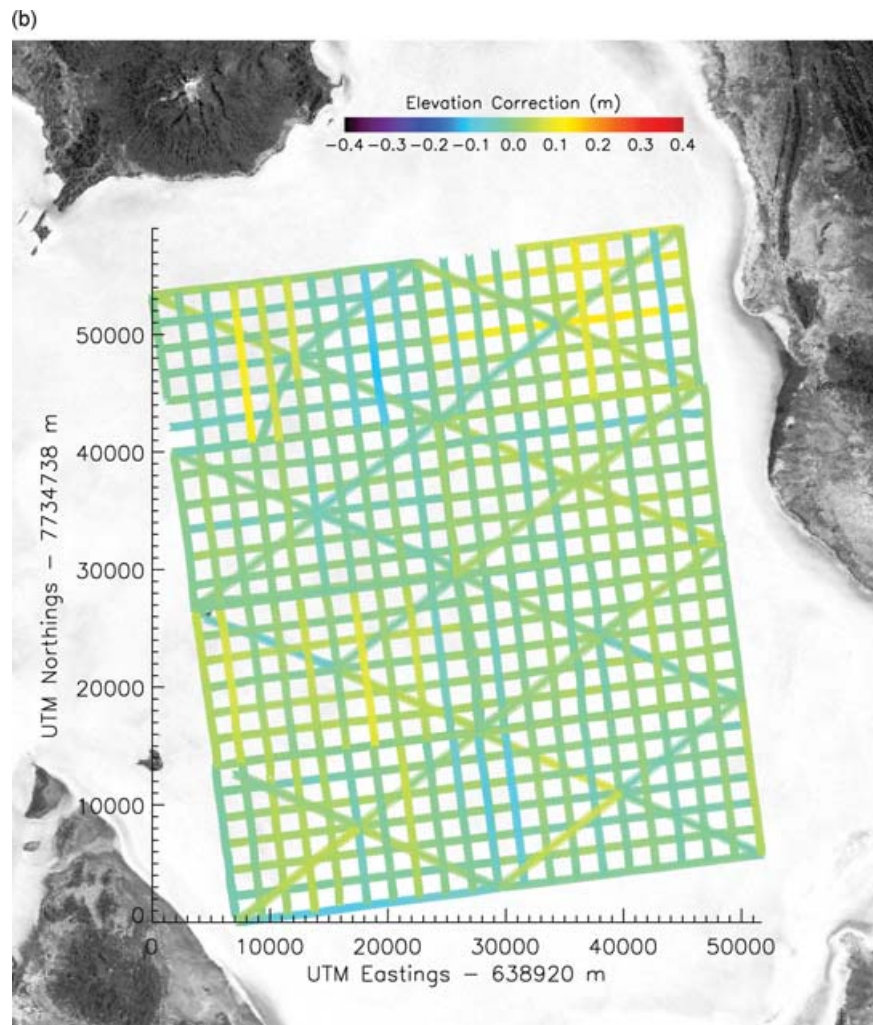
Figure 2. (*Continued*).

error in the GPS trajectory (Fig. 4). For comparison, we also fit the uncorrected survey data with the $n = 15$ basis set and obtained a misfit of 2.6 cm RMSE and temporally correlated residuals of up to 10 cm.

An independent check of survey error is provided by noise-corrected elevations from Grids 9 and 10, which we subtracted from the $n = 15$ Fourier model to obtain, respectively, misfit means of −0.4 cm and −0.1 cm and RMSEs of 1.6 and 1.5 cm. These results confirm that the salar de Uyuni GPS data acquisition and subsequent processing are consistent over the entire survey and are accurate to within the 2.2 cm rms error estimate stated earlier.

4 RESULTS AND DISCUSSION

We generated a DEM of our survey area from the Fourier model of noise-corrected kinematic GPS data (Fig. 5a). The DEM shows a complex surface with an elevation range of only 77 cm over 50 km— from a low of 3696.87 m in the broad depression along the southern boundary to a high of 3697.64 m at the northeast corner. Overplotted on Fig. 5(a) are contours of the EGM96 geoid model (Lemoine *et al.* 1998), which show that the planar SW–NE slope of the topography mimics both the direction and magnitude of the long-wavelength (≥180 km) geoid. Subtracting EGM96 geoid height values from

the DEM (i.e. converting ellipsoidal DEM elevations to orthometric elevations) removes the topographic slope and reduces the elevation range to 44 cm (Fig. 5b).

The SRTM data set also provides high-resolution orthometric elevations for the region, but these are unsuitable for characterizing the submetre level topography of the surface. SRTM elevations on the salar reveal a variety of artefacts, including short-wavelength striping perpendicular to the spacecraft ground track, anomalously low values where standing water caused low-amplitude radar returns, long-wavelength vertical oscillations, and large 'water' areas filled with uniform and inaccurate values (Fig. 6). Furthermore, the comparison between SRTM and GPS along transect A–A′ shows that SRTM elevations are digitized at 1 m increments, are biased high by ∼5 m, and range over 15 m (compared to 39 cm for the GPS). Although SRTM is the best publicly available source of topographic data for the salar and its environs, these accuracy issues make it unsuitable for characterizing the surface for satellite altimeter validation or scientific study. Similarly unacceptable for our purposes is the GTOPO30 global topography data set, which registers a single elevation value over the entire area of the GPS survey.

Returning to the topography in Fig. 5(b), we see that it is characterized by a broad ridge oriented SW–NE, with highs at both ends and flanking depressions to the north and south. Interestingly, these
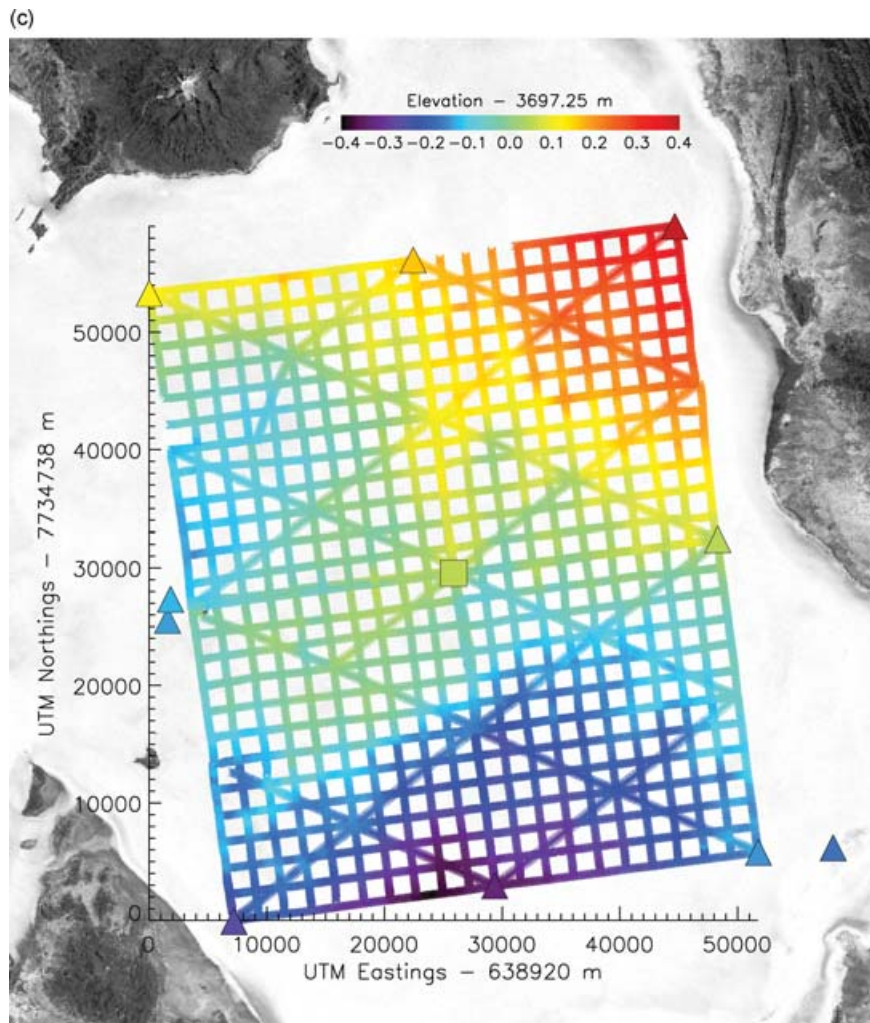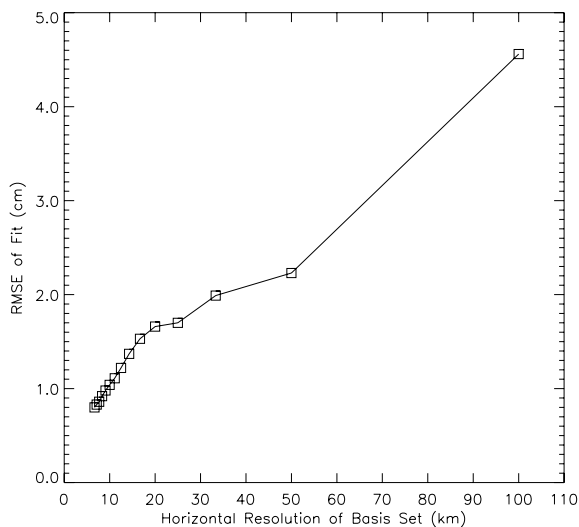
Figure 2. (*Continued*).

Figure 3. Trade-off between Fourier basis set resolution and model misfit to GPS elevation data.

features roughly correspond to mapped gravity from a local survey documented by Cady & Wise (1992) (overplotted on Fig. 5b). Of note is the topographic high at the southwest corner of the DEM which coincides with a circular gravity high centred near a rocky 'island' presumed to be the exposed peak of a buried volcanic ridge rising from the floor of the basin. The higher density of the volcanic rock with respect to the surrounding sediments alters the gravity signal at the surface, resulting in the bulls-eye pattern seen in the mapped gravity field.

Bathymetry derived from satellite images of the flooded salar (Bills *et al.* 2007) has since corroborated our observation of a correlation between salar topography and gravity. While shorter-wavelength (≤ 10 km) features of the salar DEM appear in the bathymetry, longer wavelengths and the overall slope of the DEM do not. Since water depth is the difference between the water and salar surfaces, and since water on the flooded salar nominally conforms to the geoid, this indicates that longer wavelengths in the topography conform to the geoid as well. Although the gravity field is not as smooth as the geopotential, it is similar enough to account for the gravity-topography correlation we noted earlier.

The surface of the salar de Uyuni is a cemented halite crust overlying a massive crystalline halite sedimentary unit (Fornari *et al.* 2000). From the standpoint of geomorphology, it is an unusual
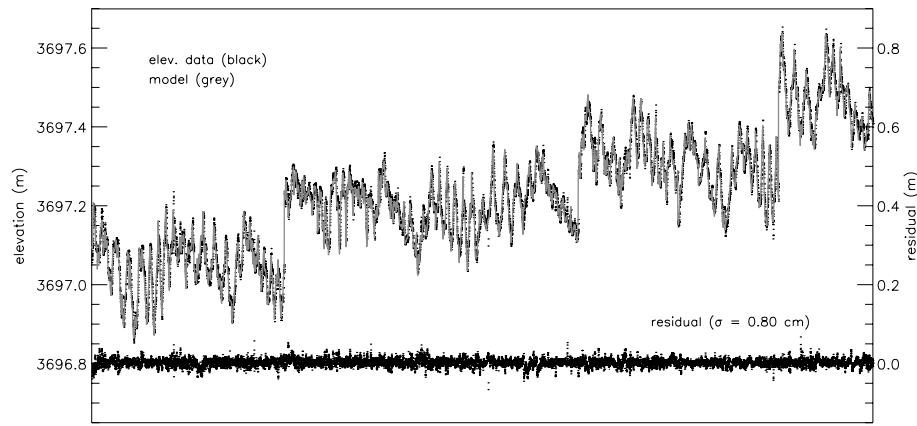
Figure 4. Comparison between the corrected survey elevation data (ordered chronologically, with successive grids appended to each other) and the $n = 15$ Fourier model. The model residuals at bottom have a standard deviation of 0.80 cm and are largely uncorrelated, indicating that there is little topography on the salar at wavelengths shorter than 6 km.
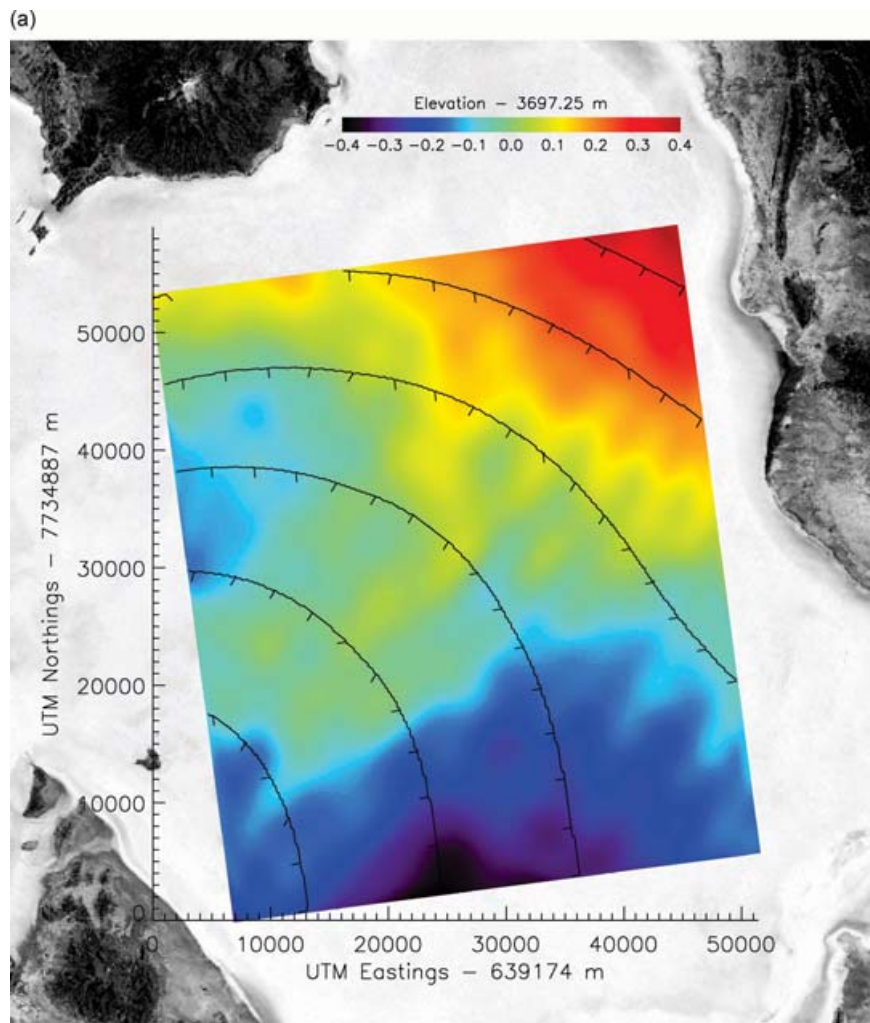

Figure 5. (a) GPS-derived digital elevation model (DEM) of the salar de Uyuni. The elevation range across the survey area is only 77 cm, more than half of which is due to the NE slope corresponding to the long-wavelength EGM96 geoid (overplotted as 5 cm contours). (b) Same as (a), but with the EGM96 geoid removed. The broad SW–NE ridge across the survey area and the depression to the SE mimic the regional gravity field (overplotted as 2 mGal contours). The gravity high to the west corresponds to a topographic high near the Isla de Pescadora (black dot to the right of the red arrow). This 'island' is the top of what is presumed to be a buried volcanic peak that would be a likely source for the gravity anomaly.
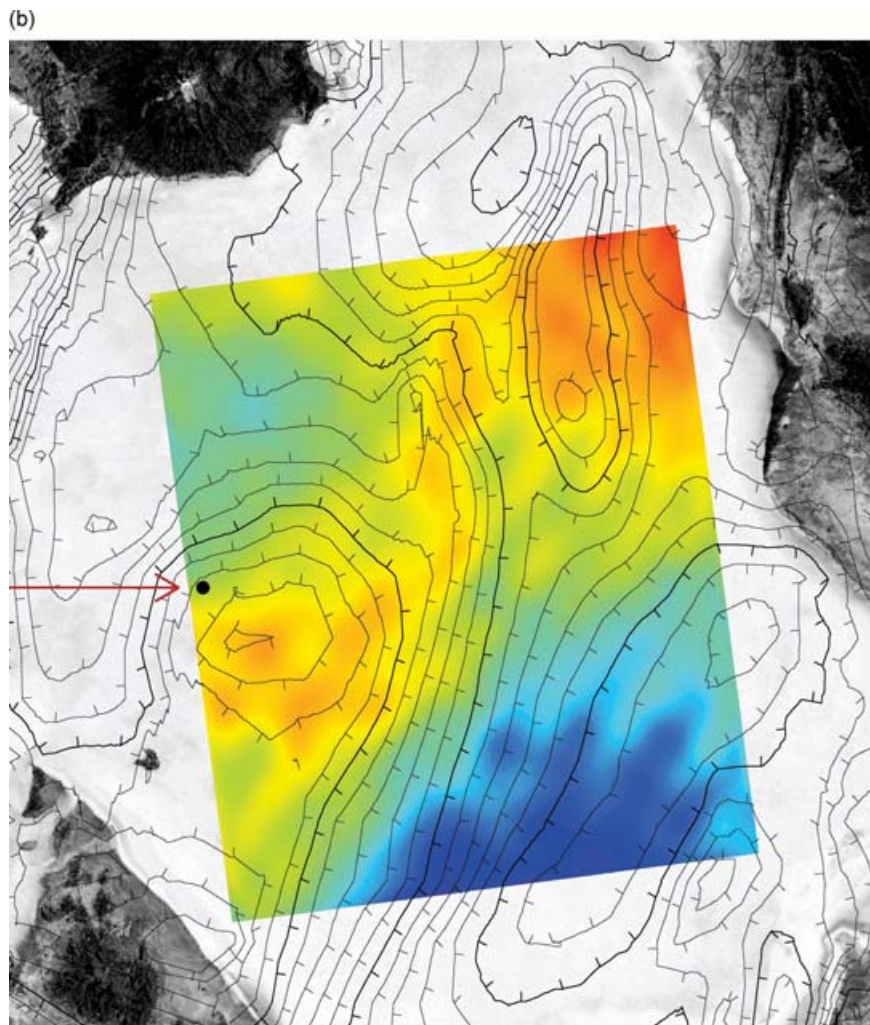
Figure 5. (*Continued*).

environment in that it is too flat to model as gravity-driven diffusion and has too little loose material available for mechanical transport to justify the use of standard models of sediment transport by wind or water. Instead, the transport of salt in solution is likely to be the primary mechanism by which surface change occurs on the salar, and we are exploring a simple model of salt transport by precipitated water to explain why salar topography might conform to the shape of the local equipotential surface (see Borsa 2005). In this model, salt is dissolved uniformly during rainstorms and flows in solution to topographic lows where it is deposited upon evaporation of the solution. The net transport of salt from orthometric highs to low points on the surface should drive the surface to an equilibrium shape that mirrors the local equipotential.

Regardless of the potential for our modelling to explain the long-wavelength topography of the salar, the local geopotential field is much too smooth to account for the short-wavelength topography of the surface. We are still trying to understand the genesis of smaller-scale surface features, most of which have persisted over the several decades for which we have satellite imagery of the salar. Future fieldwork will include new observations to help us with this effort.

REFERENCES

Argollo, J. & Mourguiart, P., 2000. Late Quaternary climate history of the Bolivian Altiplano, *Quater. Int.,* **72,** 37–51.

Baker, P.A., Rigsby, C.A., Seltzer, G.O., Fritz, S.C., Lowenstein, T.K., Bacher, N.P. & Veliz, C., 2001. Tropical climate changes at millenial and orbital timescales on the Bolivian Altiplano, *Nature,* **409,** 698–701.

Bills, B.G., Borsa, A.A. & Comstock, R.L., 2007. MISR-based passive optical bathymetry from orbit with few-cm level of accuracy on the salar de Uyuni, Bolivia, *Remote Sens. Env.,* **107,** 240–255.

Bock, Y., Nikolaidis, R.M., de Jonge, P.J. & Bevis, M., 2000. Instantaneous geodetic positioning at medium distances with the Global Positioning System, *J. geophys. Res.,* **105,** 28 223–28 253.
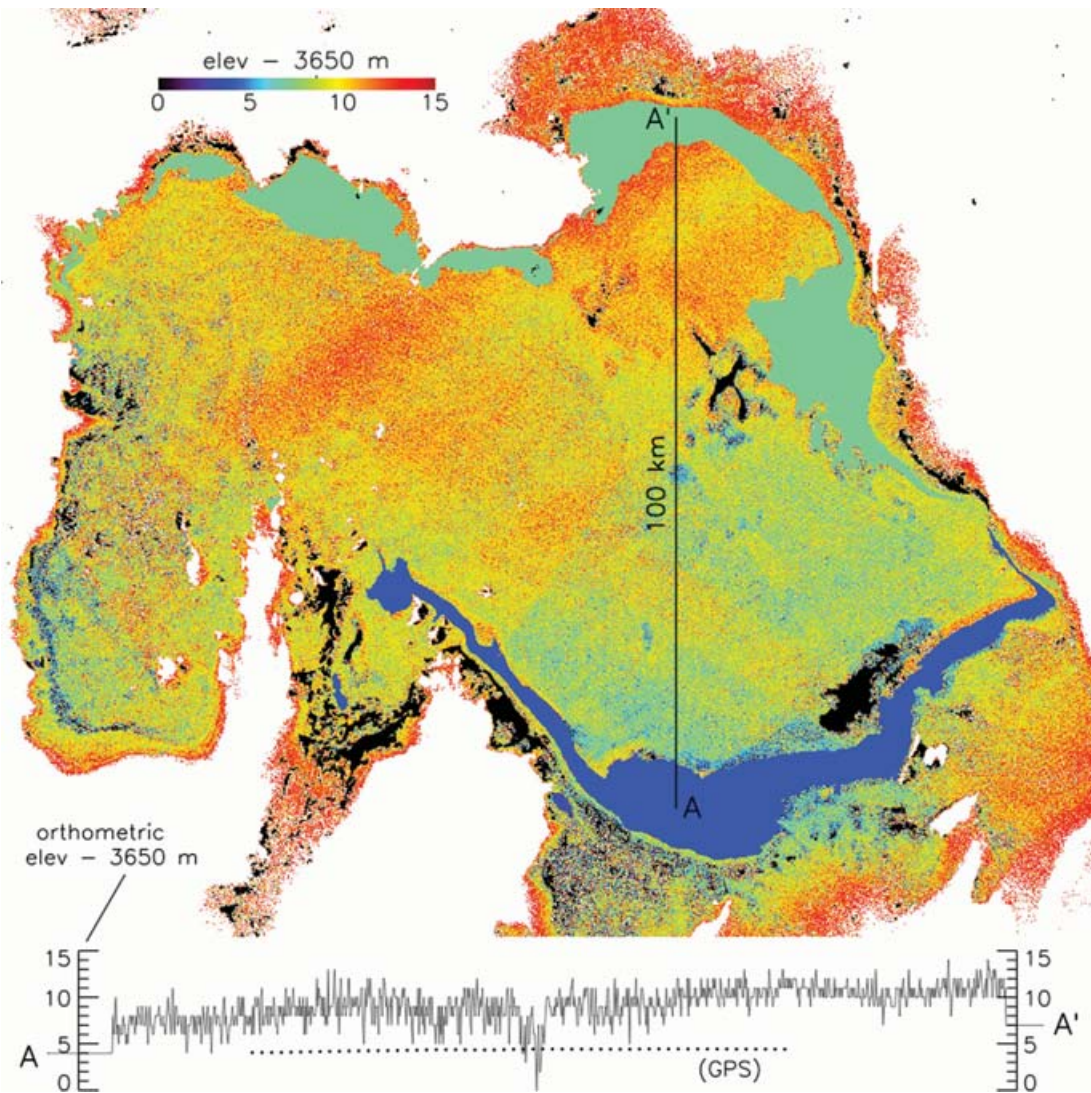
Figure 6. SRTM topography of the salar de Uyuni on April 2001, showing 15 m of apparent topography. Actual surface relief is <1 m. The plot at bottom compares SRTM elevations along the 100 km transect A–A′ with overlapping orthometric elevations from the GPS-derived DEM (dotted line), showing the large bias and variability of the SRTM data set. Examples of SRTM artefacts discussed in the text include out-of-bound returns in areas covered with standing water (black patches), areas around the perimeter of the salar identified as 'water' and given uniform and incorrect elevation values (dark blue to the south, blue-green to the north), long wavelength oscillations (e.g. the broad northeast-striking features in orange), and short wavelength striping (visible everywhere at the 1 km scale).

Borsa, A.A., 2005. Geomorphology of the Salar de Uyuni, Bolivia, *PhD thesis,* University of California at San Diego, La Jolla, CA.

Borsa, A.A., Minster, J.-B., Bills, B.G. & Fricker, H.A., 2007. Modeling long-period noise in kinematic GPS applications, *J. Geodesy,* **81,** 157–170.

Cady, J.W. & Wise, R.A., 1992. Gravity and magnetic studies, in Geology and Mineral Resources of the Altiplano and Cordillera Occidental, Bolivia, in *U.S. Geol. Surv. Bull.,* **1975,** 56–62, ed USGS.

Chen, G., 1998. GPS kinematic positioning for the airborne laser altimetry at Long Valley, California, *PhD thesis,* Massachusetts Institute of Technology, Boston, MA.

Elósegui, P., Davis, J.L., Jaldehag, R.T.K., Johansson, J.M., Niell, A.E. & Shapiro, I.I., 1995. Geodesy using the Global Positioning System: the effects of signal scattering on estimates of site position, *J. geophys. Res.,* **100,** 9921–9934.

Fornari, M., Risacher, F. & Féraud, G., 2000. Dating of paleolakes in the central Altiplano of Bolivia, *Palaeogeo., Palaeoclimatol., Palaeoecol.,* **172,** 269–282.

Fricker, H.A., Borsa, A.A., Carabajal, C.C., Quinn, K., Bills, B.G. & Minster, J.-B., 2005. Assessment of ICESat performance at the salar de Uyuni, Bolivia, *Geophys. Res. Lett.,* **32,** L21S06.

Fritz, S.C. *et al.*, 2004. Hydrological variation during the last 170,000 years in the southern hemisphere tropics of South America, *Quater. Res.,* **61,** 95–104.

Fu, L.-L., Christensen, E.J., Yamarone, C.A., Lefebvre, M., Ménard, Y., Dorrer, M. & Escudier, P., 1994. TOPEX/POSEIDON mission overview, *J. geophys. Res.,* **99,** 24 369–24 382.

James, W.R., 1966. Fortran IV program using double Fourier series for surface fitting of irregularly spaced data, *Comp. Contr., Kansas State Geol. Sur.,* **5,** 19.

King, R.W. & Bock, Y., 2006. Documentation of the GAMIT GPS analysis software v.10.21. in *GAMIT,* Massachusetts Institute of Technology and Scripps Institution of Oceanography.

Lemoine, F.G. *et al.*, 1998. The development of the joint NASA SDFC and the national imagery and mapping agency (NIMA) geopotential model EGM96. in *NASA Technical Paper*, pp. 575, GSFC, Greenbelt, Maryland.

Lowenstein, T.K. & Hardie, L.A., 1985. Criteria for the recognition of salt-pan evaporites, *Sedimentology,* **32,** 627–644.

Press, W.H., Teukolsky, S.A., Vetterling, W.T. & Flannery, B.P., 1992. *Numerical Recipes in C,* 2 edn, Vol. 1, Cambridge University Press, Cambridge, New York. pp. 623–626.

Ridgway, J.R., Minster, J.-B., Williams, N.P., Bufton, J.L. & Krabill, W.B., 1997. Airborne laser altimeter survey of Long Valley, California, *Geophys. J. Int.,* **131,** 267–280.

Risacher, F. & Fritz, S.C., 2000. Bromine geochemistry of salar de Uyuni and deeper salt crusts, Central Altiplano, Bolivia, *Chem. Geol.,* **167,** 373–392.

Rodriguez, E., Morris, C.S., Belz, J.E., Chapin, E.C., Martin, J.M., Daffer, W. & Henslet, S., 2005. An assessment of the SRTM topographic products, Technical Report JPL D-31639, pp. 143, Jet Propulsion Laboratory, Pasadena, California.

Schutz, B.E., Zwally, H.J., Shuman, C.A., Hancock, D. & DiMarzio, J.P., 2005. Overview of the ICESat Mission, *Geophys. Res. Lett.,* **32,** L21S01.

Sylvestre, F., Servant, M., Servant-Vildary, S., Causse, C., Fournier, M. & Ybert, J.-P., 1999. Lake-level chronology on the southern Bolivian Altiplano (18°-23°S) during late-glacial time and the early Holocene, *Quater. Res.,* **51,** 54–66.